

Turbulent mixing in transcritical and supercritical carbon-dioxide free-shear and boundary layer flows

Hang Song*†1, Anjini Chandra*‡1, Steven Dai*\$1, Aditya S. Ghate^{¶2}, and Sanjiva K. Lele^{¶1,2}

¹Department of Mechanical Engineering, Stanford University, Stanford, CA 94305, USA

²Department of Aeronautics & Astronautics, Stanford University, Stanford, CA 94305, USA

Supercritical fluids are used in numerous existing and developing energy technologies. The accuracy of turbulence models used with supercritical fluids is not well established due to a lack of knowledge of the coupling between the complex thermodynamics and turbulence dynamics present in turbulent supercritical flows. This study aims to provide fundamental characterization of turbulent momentum and heat transfer in supercritical flows through two canonical flows: the free shear layer flow and the zero-pressure-gradient boundary layer. Direct numerical simulations using high-order compact finite difference methods are performed with real-gas equation-of-state and transport models. The simulation results indicate that the real-gas behavior influences the turbulent fluctuations of thermodynamic quantities. Besides the non-dimensional parameters used for characterizing the turbulent flow of an ideal gas, an extra parameter is needed to identify the thermodynamic state of the fluid. The results also indicate that the classic turbulent scalings observed in the velocity fields exhibit behaviors similar to those found in ideal-gas flows.

I. Introduction

Supercritical carbon dioxide (sCO₂) plays an increasingly important role in the design of modern compact power systems [1]. A pure fluid becomes supercritial when both its pressure and temperature are above the critical condition. At the supercritical pressure, the fluid transitions between subcritical and supercritical states and undergoes a pseudo phase change. During the pseudo phase change, a drastic change in density and large internal energy variation occur within a relatively small change in temperature about the critical value. These thermodynamic phenomena are widely utilized in the design of modern compact power systems to boost the efficiency of the systems while maintaining a compact system size. For example, one major application of supercritical sCO₂ is to power cycles, such as the sCO₂ Brayton cycle, where sCO₂ plays an important role in heat transfer [2, 3]. The sCO₂ Brayton cycle is appealing due to its higher thermal efficiency, compactness, and adaptability in operating with other heat sources, such as solar power, nuclear reactors, and fossil fuels, compared to existing power cycles [4, 5].

Due to the complex thermodynamic behavior of a fluid near the critical condition, the flow dynamics and heat transfer performance for supercritical flows differ significantly from those for an ideal gas compressible flow or a flow in the incompressible regime. In applications to power systems, such as the sCO₂ Brayton cycle, the coupling between complex thermodynamics and turbulence dynamics impacts the performance of the cycle and poses a challenge in studying the physics associated with the flow structures within the cycle. Fundamental investigations of turbulent canonical flows, including shear and boundary layers, near the critical condition will provide useful insights for the development of Reynolds-Averaged-Navier-Stokes (RANS) and subgrid-scale (SGS) models used for low-cost predictive simulations, reduced-order modeling for flow control, and system optimization.

Previous work in supercritical shear layer DNS simulations have indicated that modifications to existing SGS models are necessary to accurately capture real gas effects [6]. Recent LES simulations of spatially developing shear layers further emphasized the need to develop new models that account for the complex coupling between thermodynamics and turbulence [7]. Many simulations conducted so far have required additional treatment [6, 8], such as filtering, to

^{*}These authors equally contributed to this work.

[†]Ph.D. Candidate, Department of Mechanical Engineering, Stanford University. AIAA Member. (Songhang@stanford.edu)

[‡]Ph.D. Candidate, Department of Mechanical Engineering, Stanford University. AIAA Member. (🖂 achandr3@stanford.edu)

[§]Ph.D. Candidate, Department of Mechanical Engineering, Stanford University. AIAA Member. (Stanford.edu)

[¶]Ph.D. Alumni, Department of Aeronautics & Astronautics, Stanford University. AIAA Member. (aditya90@stanford.edu)

^{||} Edward C. Wells Professor, Department of Aeronautics & Astronautics and Department of Mechanical Engineering, Stanford University. AIAA Associate Fellow. (☑ lele@stanford.edu)

preserve numerical stability. In addition, experiments for supercritical jets and planar shear layer have been conducted, but they provide limited insight into the physics associated with supercritical flows due to limitations on measurements and the extreme physical conditions needed to maintain supercritical flows [9]. For boundary layer configuration, previous simulations relied on existing turbulence models or were limited to low-Mach regimes, far from the operating conditions expected for many developing applications [10, 11].

This work utilizes a high-fidelity computational framework to study supercritical shear and boundary layers. The computational framework extends a similar framework for ideal gases to include complex thermodynamic and transport relations that capture the behavior of a fluid around the critical point. The framework also enables simulations of supercritical flows without additional treatments to preserve numerical stability. A database for supercritical shear layer and boundary layer flows will be established from which turbulent statistics and other quantities can be computed. These quantities can then be compared to established results for canonical shear and boundary layer cases for ideal gases [12].

II. Simulation configuration details

A. Physical formulation

All the simulations presented in this work numerically solve the compressible Navier-Stokes equations and enforce conservation of mass, momentum and total energy. The governing system of equations is provided in index notation form as follows:

$$\frac{\partial \rho}{\partial t} + \frac{\partial \rho u_j}{\partial x_i} = 0 \tag{1}$$

$$\frac{\partial \rho u_i}{\partial t} + \frac{\partial}{\partial x_i} \left(\rho u_i u_j + p \delta_{ij} \right) = \frac{\partial \sigma_{ij}}{\partial x_i} \tag{2}$$

$$\frac{\partial \rho e_{\text{tot}}}{\partial t} + \frac{\partial}{\partial x_j} \left[\left(\rho e_{\text{tot}} + p \right) u_j \right] = \frac{\partial}{\partial x_j} \left(u_i \sigma_{ij} - q_j \right) \tag{3}$$

where ρ is the density field, u_i is the velocity vector field, p is the pressure field, δ_{ij} is the identity tensor, σ_{ij} is the viscous stress tensor, e_{tot} is the specific total energy, and q_j is the heat flux. The viscous stress tensor is calculated as

$$\sigma_{ij} = 2\mu S_{ij} - \frac{2}{3}\mu S_{kk}\delta_{ij} \tag{4}$$

where μ is the dynamic shear viscosity and S_{ij} is the rate of strain tensor defined as $S_{ij} = (u_{i,j} + u_{j,i})/2$. The formulation neglects the bulk viscosity. The total specific energy consists two components:

$$e_{\text{tot}} = e + u_i u_i / 2$$

where e is the specific internal energy and $u_j u_j / 2$ is the specific kinetic energy. The heat flux q_j is calculated based on Fourier's law of thermal conduction as

$$q_j = -\lambda \frac{\partial T}{\partial x_j} \tag{5}$$

where λ is the thermal conductivity and T is the temperature field. The system is closed by giving the equations of state (EOS) that formulate the pressure-specific-volume-temperature (p-v-T) relation as well as the calculation of the internal energy and the models of transport properties.

For a dense gas near the critical condition, the Peng-Robinson EOS [13] is used as the p-v-T relation. The dimensionless expression is given in the following equation:

$$p_r = \frac{T_r}{v^* - b^*} - \frac{a^* \alpha(T_r)}{v^{*2} + 2v^* b^* - b^{*2}}$$
 (6)

where p_r and T_r are the reduced pressure and temperature respectively. Given the critical pressure p_c and the critical temperature T_c , p_r and T_r are defined as $p_r = p/p_c$ and $T_r = T/T_c$. $v^* = p_c v/(RT_c)$ is the nondimensional specific volume where R is the specific gas constant and $v = 1/\rho$ is the specific volume. Both a^* and b^* are constants, and α is a dimensionless function of T_r :

$$a^* = 0.45723553$$
 $b^* = 0.07779607$ $\alpha(T_r) = \left[1 + \kappa \left(1 - \sqrt{T_r}\right)\right]^2$

where κ is a function of the acentric factor of the gas molecule, ω , and is given as:

$$\kappa = 0.37464 + 1.54226\omega - 0.26992\omega^2$$

In this work, the targeted working fluid is CO_2 . The acentric factor is set to $\omega = 0.239$. The p-v-T behavior predicted by Peng-Robinson EOS model is shown in Fig. 1, and the results are compared with open-source data from the National Institute of Standards and Technology (NIST) WebBook [14] for validation.

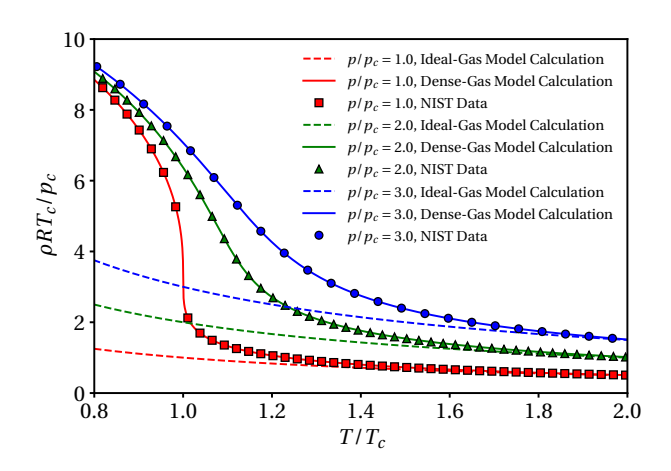


Fig. 1 p-v-T relation of CO_2 near the critical condition. The curves are calculated from the Peng-Robinson EOS model, and the symbols are extracted from the NIST database.

The internal energy is calculated by integrating along an isochoric path followed by an isothermal path as shown in the following equation:

$$e = e_{\text{ref}} + \int_{T_{\text{ref}}}^{T} c_{\nu}(T, \nu_{\text{ref}}) dT + \int_{\nu_{\text{ref}}}^{\nu} \left[T \left(\frac{\partial p}{\partial T} \right)_{\nu} - p \right] d\nu \tag{7}$$

where the subscript "ref" denotes the reference state and c_v is the isochoric specific heat. In Eq. (7), the second integral can be calculated based on the Peng-Robinson EOS p-v-T relation, but the first integral requires a model for $c_v(T,v)$. For simplicity, the reference state is selected in the ideal gas limit by taking $v_{\rm ref} \to \infty$ and $T_{\rm ref} = 0$ so that $e_{\rm ref}$ can be set to zero and c_v only depends on T. For CO₂, $c_v(T,\infty)$ is calculated based on a power law fitting.

$$c_{\nu}(T, \infty) = c_{\nu}(T_{\text{ref}}, \infty) \left(\frac{T}{T_{\text{ref}}}\right)^{n} \tag{8}$$

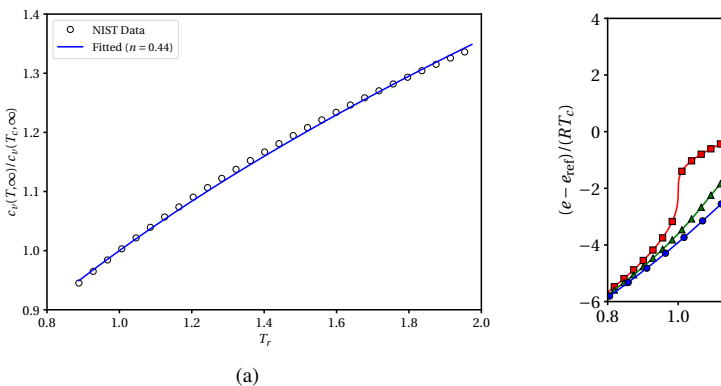
where the parameter n is set to n = 0.44 for the best fit within the regime of interest. The EOS models for internal energy calculation are also validated using the NIST database [14], and the results are shown in Fig. 2.

The dynamic shear viscosity and thermal conductivity are calculated based on the Chung et al. model [15]. The detailed implementation is provided in Ref [15] and Ref [16]. A consistent non-dimensionalization is proposed by the authors in Ref [17]. Given the p-v-T relation, the conceptual forms of the transport models can be equivalently expressed as

$$\mu = \mu_{\text{ref}} G_{\mu}(T_r, p_r)$$
 and $\lambda = R \mu_{\text{ref}} G_{\lambda}(T_r, p_r)$ (9, 10)

where μ_{ref} is a reference viscosity, and G_{μ} and G_{λ} are both dimensionless functions considering the thermodynamic state and the gas molecular structure.

Consistent with the dense gas EOS models, p_c and T_c naturally impose the pressure and temperature scales for non-dimensionalization. Correspondingly, the density scale can be defined as $\rho_0 = p_c/(RT_c)$ according to dimensional analysis. Additionally, a velocity scale can be introduced as $U_0 = \sqrt{RT_c}$. As a result, the dimensionless pressure and temperature are identical to the reduced pressure and temperature respectively, but ρ_0 and U_0 , as obtained from the dimension analysis, are not directly related to the quantities at the critical condition. μ_{ref} in the transport models can be set to match the targeted Reynolds number in the simulation. For a certain gas, the behavior of the thermal conductivity is paired with the dynamic shear viscosity as shown in Eq. (10) so that the Prandtl number is inherently determined by the fluid's thermodynamic state.



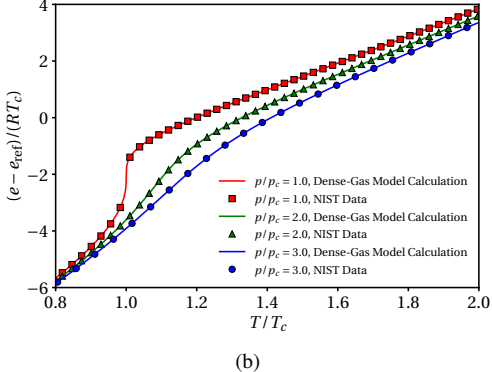


Fig. 2 Validation of internal energy calculation for CO_2 near the critical condition: (a) calculation of the isochoric specific heat in the ideal gas limit, and (b) calculation of the specific internal energy. The curves represents the calculation results using the proposed EOS models and the symbols are extracted from the NIST database.

B. Numerical methods

The simulations in this work are calculated using sixth-order compact finite difference methods [18, 19] arranged in a collocated-variable-storage-staggered-flux-assembly framework [20] for high-order grid convergence and high spectral resolution. For simulations of shock-free flows, no non-physics-based artificial properties or solution filtering are needed to preserve numerical stability. For high-speed flows, when shocks are present, the fifth-order weighted essentially non-oscillatory (WENO5-JS) interpolation scheme [21] is combined with the Rusanov type Riemann flux [22]. The shock capturing scheme is locally activated by a modified Ducros shock sensor, ϕ , which acts as an indicator to trigger activation. The expression for ϕ is given in the following equation.

$$\phi = \frac{-\theta|\theta| + \varepsilon^2}{\theta^2 + \omega \cdot \omega + \varepsilon^2} \tag{11}$$

where $\theta = \nabla \cdot \boldsymbol{u}$ is the velocity dilatation, $\boldsymbol{\omega} = \nabla \times \boldsymbol{u}$ is the vorticity vector, and $\boldsymbol{\varepsilon}$ is set to 1×10^{-16} for numerical regularization. A threshold sensor value is specified as $\phi_{TH} = 0.4$. When $\phi > \phi_{TH}$, the shock capturing scheme is activated, and only central-fluxes are used everywhere else.

1. Simulation configuration of the planar shear layer

The simulation configuration of the planar shear layer is shown in Fig. 3, where streamwise direction is in x and the transverse direction is in y. The computational domain is periodic in the x- and z- directions, and the computational mesh is uniform along these two directions. The computational mesh is stretched along the y-direction with higher grid resolution near the center plane to resolve the growth of the shear layer there. Numerical sponge layers are applied near both boundaries in y-direction to impose the far-field free-stream conditions. The initial condition is prescribed at a numerically regularized smooth thin shear layer profile. The flow outside the initial thin shear profile on each side is at the free-stream condition.

The flow is characterized by the density ratio $\rho_{+\infty}/\rho_{-\infty}$ and the turbulent Mach number M_c defined as

$$M_c = \frac{|U_{+\infty} - U_{-\infty}|}{c_{+\infty} + c_{-\infty}} \tag{12}$$

where $U_{+\infty}$ and $U_{-\infty}$ are the streamwise velocity component in free-stream on each side respectively, and $c_{+\infty}$ and $c_{-\infty}$ are the free-stream speed of sound on each side respectively. In this work, $U_{+\infty}$ and $U_{-\infty}$ are configured such that

$$\rho_{+\infty}U_{+\infty} + \rho_{-\infty}U_{-\infty} = 0 \tag{13}$$

For simplicity, the definition $\Delta U_{\infty} = U_{\infty} - U_{-\infty}$ is used in the analysis.

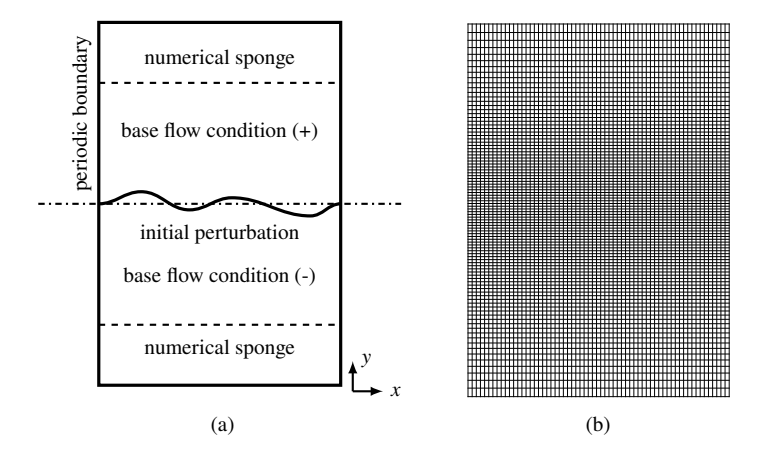


Fig. 3 Simulation configuration of compressible planar shear layer: (a) configuration of computational domain; (b) computational mesh. The computational domain is periodic in z-direction, and the computational mesh is uniform in x and z.

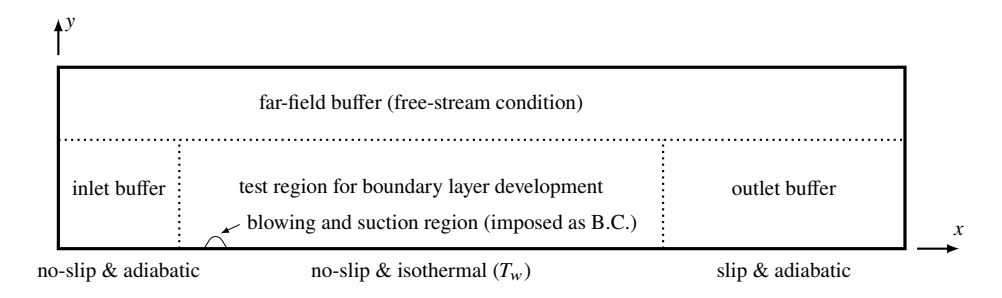


Fig. 4 Simulation configuration of turbulent boundary layer flow.

2. Simulation configuration of the zero-pressure-gradient boundary layer

The simulation configuration of the zero-pressure-gradient boundary layer is shown in Fig. 4. The computational domain is divided into four regions. The measurements are taken in the test region where the computational mesh is uniform in the x- and z- directions and clustered in the y- direction to resolve the full range of length scales within the turbulent boundary layer. The computational mesh is highly coarsened along the streamwise direction in the inlet and outlet buffer regions away from the test region. The flow in the inlet buffer is regularized using the numerical sponge. The flow in the outlet buffer is regularized using the WENO5-JS interpolation combined with the Riemann flux as used for shock capturing. The streamwise boundary condition on the outlet side uses first-order extrapolation. The flow in the far-field buffer is regularized at the free-stream condition using the numerical sponge.

III. Planar shear layer

In this work, simulations of eight different cases are performed to investigate the effects of Mach number and real-gas thermodynamics. All simulations used in this work have same free-stream pressure $p_r = 3$ and density ratio, $\rho_{+\infty}/\rho_{-\infty} = 2$. Different combinations of free-stream temperatures are selected to satisfy the pressure and density ratio constraints. Unlike the ideal gas, the thermodynamic behavior of a dense gas strongly depends on the absolute temperature. Due to the temperature difference, heat transfer occurs associated with the development of the turbulent shear layer. Recent works by Vadrot et.al [23, 24] examined compressible temporal shear layers with dense gas effects, but in their simulations the thermodynamic conditions are identical for the upper and lower streams. The detailed configurations of the simulations used in the analysis are listed in Table 1. The flow visualizations of the turbulent shear layer at low and high convective Mach numbers using numerical Schlieren imaging are shown in Fig. 5. Associated with the growth of the turbulent shear layer at a high M_c , the flow contains Mach waves and shock waves due to the compressibility effects. The visualizations of density fields are shown in Fig. 6. Consistent with the numerical Schlieren

imaging, significantly larger density fluctuation are observed in the high M_c case (PSL00). The profile of planar averaged density is shown in Fig. 7a where the coordinate in the transverse direction (y) is shifted to the momentum center-plane y_c where the planar mean momentum is zero. For reference, the planar-averaged density-weighted velocity dilatation $(\rho \nabla \cdot \boldsymbol{u})$ is shown in Fig. 7b. Based on the Lagrangian form of the mass conservation

$$\left(\frac{\partial \rho}{\partial t} + u_j \frac{\partial \rho}{\partial x_j}\right) + \rho \frac{\partial u_j}{\partial x_j} = 0$$

The profile provides an insight into the thermodynamic variation of a fluid parcel. Comparing with the density profile, it shows that the heat transfer within the turbulent shear layer in cases PSL01, PSL03, and PSL07 primarily causes local expansion of the denser fluid. As observed directly from the plots shown in Fig. 7, the peak expansion occurs slightly on the lower-density side defined by the zero-momentum center-plane. Moreover, the free-stream temperatures in PSL07 straddle the pseudo-critical temperature (Widom point) at the free-stream pressure which is defined by the temperature associated with the local maximum isobaric specific heat. Pseudo-phase change occurs within the mixing layer. For the configuration specified in PSL07, the pseudo-phase change suppresses the thermal expansion compared to the other two cases (PSL01 and PSL03) shown in Fig. 7. Mean velocity profile shown in Fig. 7c shows that established scaling for velocity profile of ideal gas mixing layers is applicable for dense gas mixing layers and no additional scaling is needed.

Case ID	M_c	p_r	$T_{-\infty}/T_c$	$T_{+\infty}/T_c$	$\rho_{+\infty}/\rho_{-\infty}$	line style
PSL00	1.0	3	1.40	2.16	2	red dotted
PSL01	1.0	3	1.60	2.73	2	red solid
PSL02	1.0	3	2.00	3.78	2	red dashed
PSL03	0.2	3	1.20	1.59	2	black dashdot
PSL04	0.2	3	1.40	2.16	2	black dotted
PSL05	0.2	3	1.60	2.73	2	black solid
PSL06	0.2	3	2.00	3.78	2	black dashed
PSL07	0.2	3	1.10	1.39	2	blue dashed

Table 1 Setups of planar shear layer simulations.

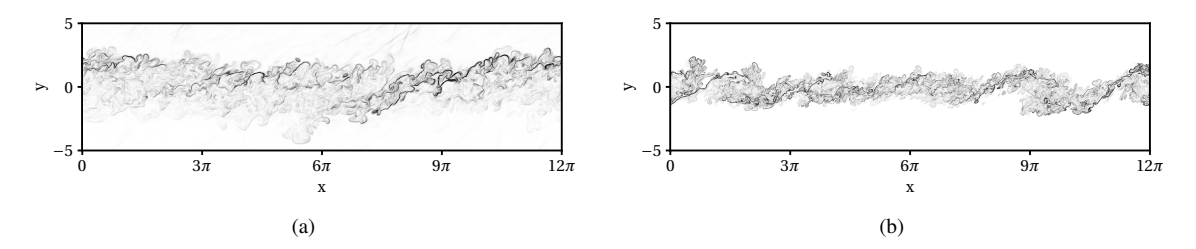


Fig. 5 Numerical Schlieren imaging of (a) PSL01 and (b) PSL07.

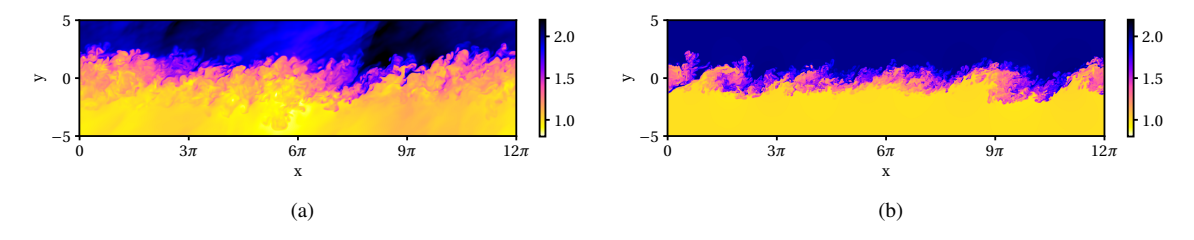


Fig. 6 Density visualization of (a) PSL01 and (b) PSL07.

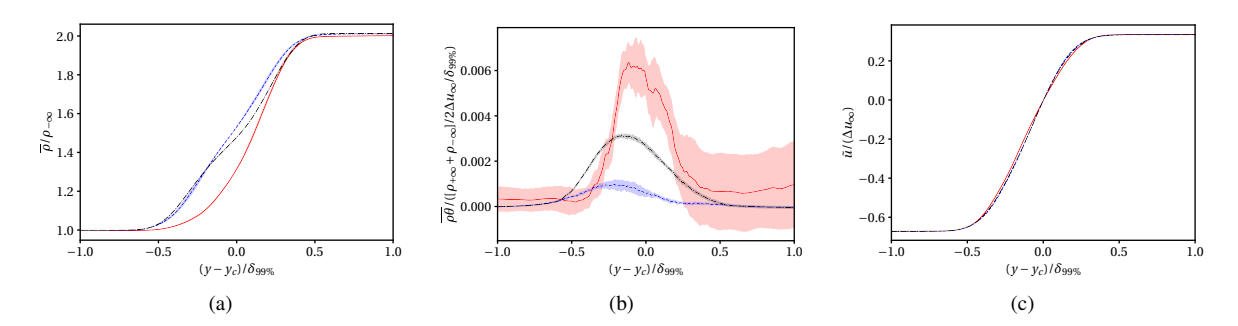


Fig. 7 Planar averaged profiles of (a) density, (b) dilatation and (c) streamwise velocity across the turbulent shear layer: PSL01 (red), PSL03 (black), and PSL07 (blue).

The one-dimensional velocity energy spectra in the stream-wise (x) and span-wise (z) directions are shown in Fig. 8. Comparing with the $k^{-5/3}$ reference scaling, it can be seen that the turbulent velocity fluctuation along the homogeneous directions follows the same scaling as used in incompressible and ideal-gas turbulence. Several selected Reynolds stress components (normalized), u''u'', v''v'', w''w'', and u''v'' are also provided in Fig. 9 for reference, where the operators " (\cdot) " and " (\cdot) " are defined as planar Reynolds and Favre averaging respectively and the fluctuating components are denoted as " $(\cdot)'' = (\cdot) - (\cdot)$ ". The profile shown in Fig. 9 are normalized using the free-stream velocity difference, ΔU_{∞}^2 . The profiles of the Reynolds stresses show consistent behaviors as observed in the simulations of ideal gas compressible turbulent shear layer variable density mixing [25, 26].

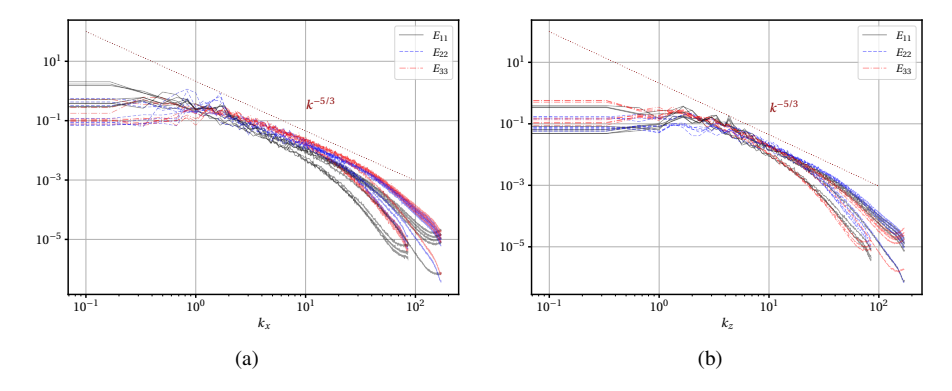


Fig. 8 1D velocity energy spectra in the turbulent planar shear layer flow of all cases listed in Table 1. The velocity energy spectra is measured at the center plane, y_c , where the mean momentum is zero.

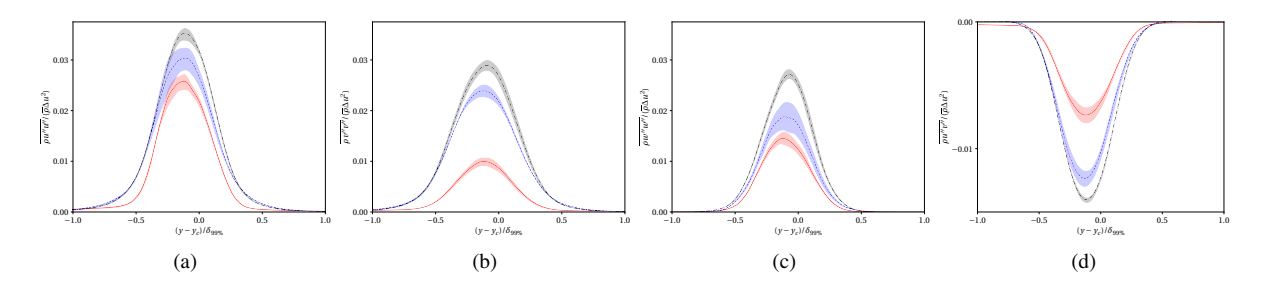


Fig. 9 Normalized Reynolds stresses across the shear layer: PSL01 (red), PSL03 (black), and PSL07 (blue).

The growth of the momentum thickness and fluctuations of the pressure and temperature fields are shown in Fig. 10,

where The operator " $\langle (\cdot) \rangle$ " denotes the domain averaging defined as

$$\langle (\cdot) \rangle = \frac{1}{\delta^{**}} \int_{-\infty}^{+\infty} \overline{(\cdot)} dy$$

All data in the plots in Fig. 10 have the same free-stream density ratio and include only two Mach numbers. The growth of the momentum thickness in Fig. 10a shows self-similar behaviors parametrized by the Mach number. The evolution of density and temperature fluctuations plotted in Fig. 10b and Fig. 10c suggests the effects of Mach number. However, the profiles do not agree well to show strong similarity behaviors. The absence of the similarity behavior in Fig. 10b and

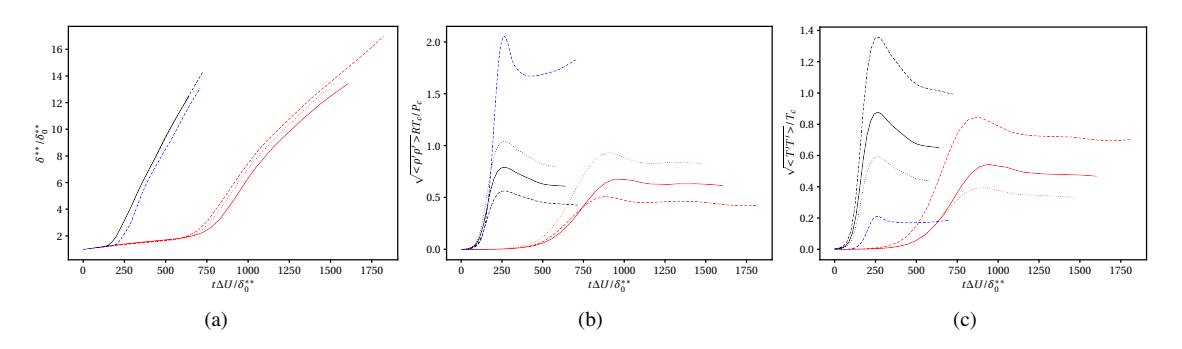


Fig. 10 Time evolution of statistics within planar shear layer: (a) momentum thickness, (b) density fluctuation, and (c) temperature fluctuation.

Fig. 10c is due to the non-similar behavior of the real-gas EOS model. Unlike the ideal gas model, the real-gas EOS model scales relative to a fixed thermodynamic state, such as the critical point. Therefore, extra parameter needs to be introduced to the scaling. As an attempt, the compressibility factor $Z = p/(\rho RT)$ is used, where for ideal gases Z = 1. Towards the small fluctuating limit, a linearized p-v-T model for the fluctuating quantities can be written as

$$p' \approx ZR\left(\overline{\rho}T^{\prime\prime} + \rho^{\prime}\widetilde{T}\right) \tag{14}$$

Compared to that from the ideal gas case, the density and temperature fluctuation in response of the same pressure fluctuation is off back a factor of Z. Inspired from this analysis, a simple and convenient scaling using the information from free-stream conditions on both sides for density and temperature fluctuation can be designed as

$$\rho_s = \frac{2p_{\infty}}{R\left(Z_{-\infty}T_{-\infty} + Z_{+\infty}T_{+\infty}\right)} \quad \text{and} \quad T_s = \frac{2\Delta T_{\infty}}{Z_{-\infty} + Z_{+\infty}}$$
(15)

where ρ_s and T_s are the density and temperature scales respectively. As shown in Fig. 11, the rescaled density fluctuation and temperature fluctuation curves collapse much more tightly than the unscaled curves for all cases with freestream temperature above the pseudo-critical point. The case with freestream temperatures straddling the pseudo-critical point satisfies the scaling in the profile of density fluctuations, but is unable to follow the similarity behavior after re-scaling.

IV. Turbulent boundary layer

In addition to simulations of compressible shear layers, simulations of zero-pressure-gradient, turbulent boundary layers with different wall and freestream temperatures were run. The simulations include one case with wall and freestream temperatures below the Widom line temperature corresponding to $p_r = 3$, three cases with wall and freestream temperatures straddling the Widom line, and one case with both temperatures above the Widom line. Table 3 summarizes all cases run.

Line plots of averaged transport, thermodynamic, and streamwise velocity profiles for all five cases are shown in Fig. 14. The profiles are plotted in the *y-z*-plane and normalized by corresponding freestream quantities for each case. The temperature, kinematic viscosity, and density profiles show that for each plot, the curves representing transcritical temperature conditions exhibit similar trends with increasing normalized *y*-coordinate. These trends differ from trends in the cases corresponding to subcritical and supercritical temperature conditions. In addition, the profiles corresponding

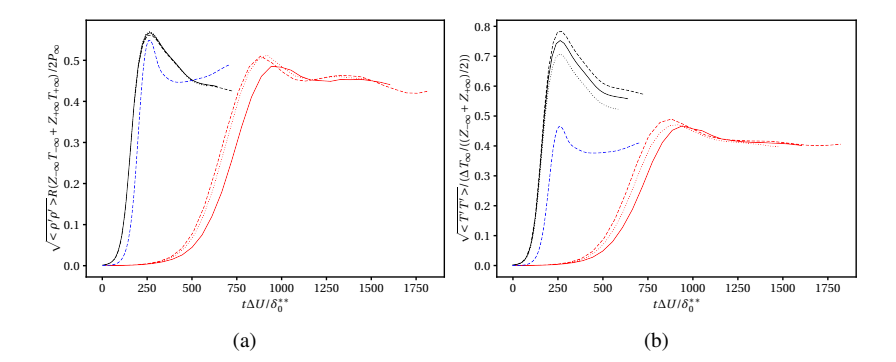


Fig. 11 Re-normalized density and temperature fluctuation profiles.

Case ID	M_{∞}	p_r	T_w	T_{∞}	line style
TBL00	0.3	3	0.75	1.05	navy solid
TBL01	0.3	3	0.75	1.50	blue dashed
TBL02	0.3	3	0.90	1.50	red dashdot
TBL03	0.3	3	0.95	1.50	gray solid
TBL04	0.3	3	1.20	1.50	maroon dashdot

Table 2 Parameters used in boundary layer simulations.

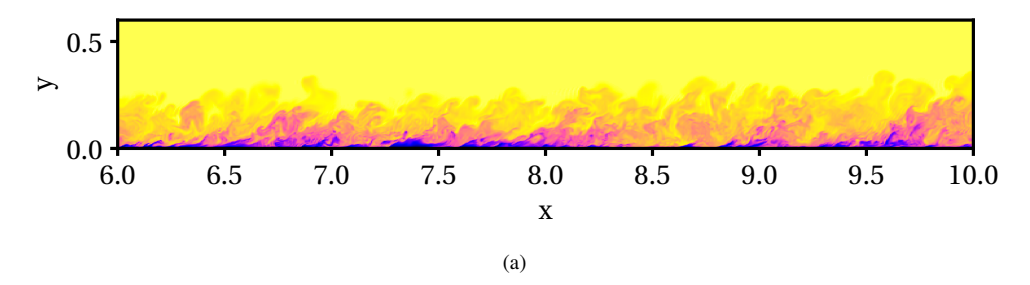


Fig. 12 Visualizations of density of the boundary layer flow in x-y plane for the condition $p_r = 3$, $T_{\infty} = 1.5$, and $T_w = 0.75$

to transcritical conditions exhibit sharp gradients in transport properties near the wall. The profiles suggest that the presence of the Widom line within the turbulent boundary layers, a phenomenon that occurs under transcritical wall and freestream temperature conditions, alters transport profiles near the wall.

Fig. 15 shows the Reynolds-averaged shear stresses $\overline{\rho u''u''}$, $\overline{\rho u''v''}$, $\overline{\rho v''v''}$, and $\overline{\rho w''w''}$ in the *y-z*-plane of the boundary layer normalized by the wall shear stress τ_w , or semi-local scaling, as outlined by Trettel & Larsson [27]. Recent studies have used the semi-local normalization to scale the Reynolds shear stresses for turbulent flows under transcritical conditions. For instance, Sciacovelli et al. [28] and Kim et al. [29] studied transcritical, turbulent channel flows at supersonic and low-Mach conditions respectively. Kim et al. found a tight collapse of the Reynolds shear stresses using semi-local scaling while Sciacovelli et al. showed a collapse that aligned the peak locations of the Reynolds stress curves along y^* [28, 29] but not the peak values. The expression for the semi-locally scaled wall coordinate y^* is given as

$$y^* = \frac{\sqrt{\tau_w/\overline{\rho}}}{\overline{\mu}/\overline{\rho}}y\tag{16}$$

The semi-local normalization in Fig. 15 does appear to collapse the Reynolds shear stresses for the five cases in this paper; however, the collapse is not as tight as those from the literature [28, 29].

Fig. 16 shows the evolution of the collapse of mean velocity profiles for the five cases using the classical wall, Van

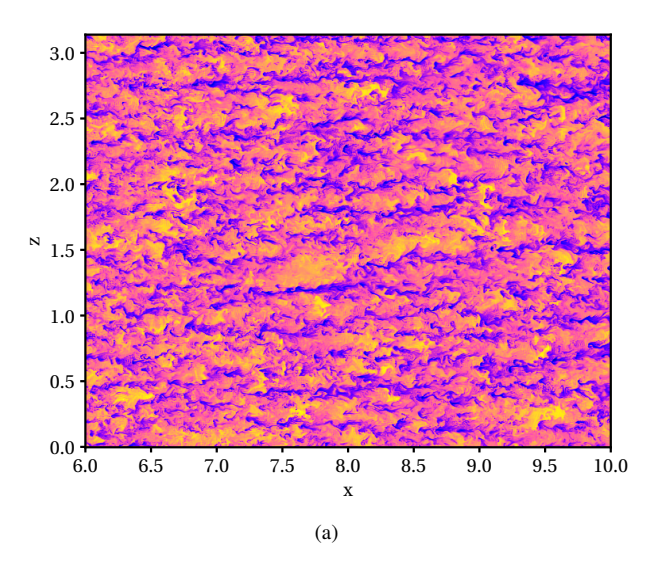


Fig. 13 Visualizations of density of the boundary layer flow in x-z plane for the condition $p_r = 3$, $T_{\infty} = 1.5$, and $T_w = 0.75$

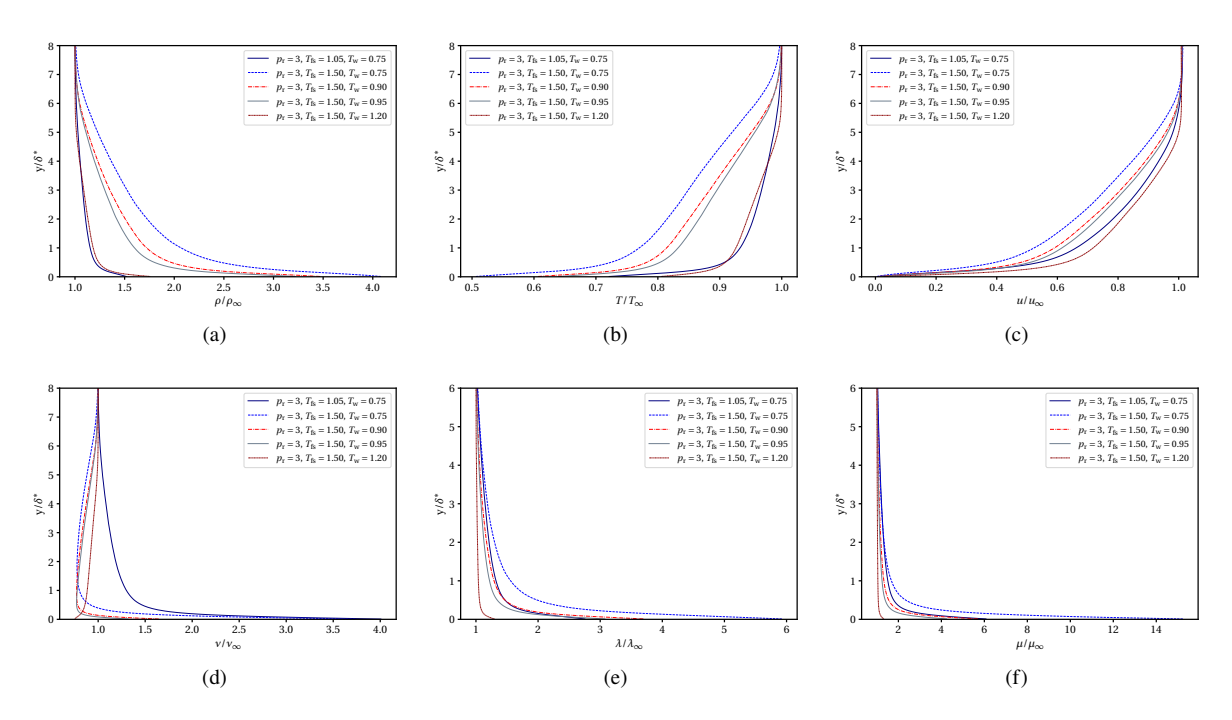


Fig. 14 Plots of mean transport, thermodynamic, and streamwise velocity profiles in the boundary layers averaged over time and the z-direction: (a) density, (b) temperature, (c) streamwise velocity, (d) kinematic viscosity, (e) thermal conductivity, and (f) dynamic viscosity.

Driest, and Trettel & Larsson scalings [27]. The profiles collapse most tightly for the Trettel & Larsson scaling which extends the Van Driest scaling by accounting for flows with strong wall heat flux [27]. However, as with the plots of scaled Reynolds shear stresses, the collapse is not as tight as the one presented by Sciacovelli et al. [28]. Fig. 15 and 16 suggest that additional scaling may be necessary to fully collapse the Reynolds shear stress and streamwise velocity profiles especially across cases where the Widom line is present within the boundary layer and where it is not.

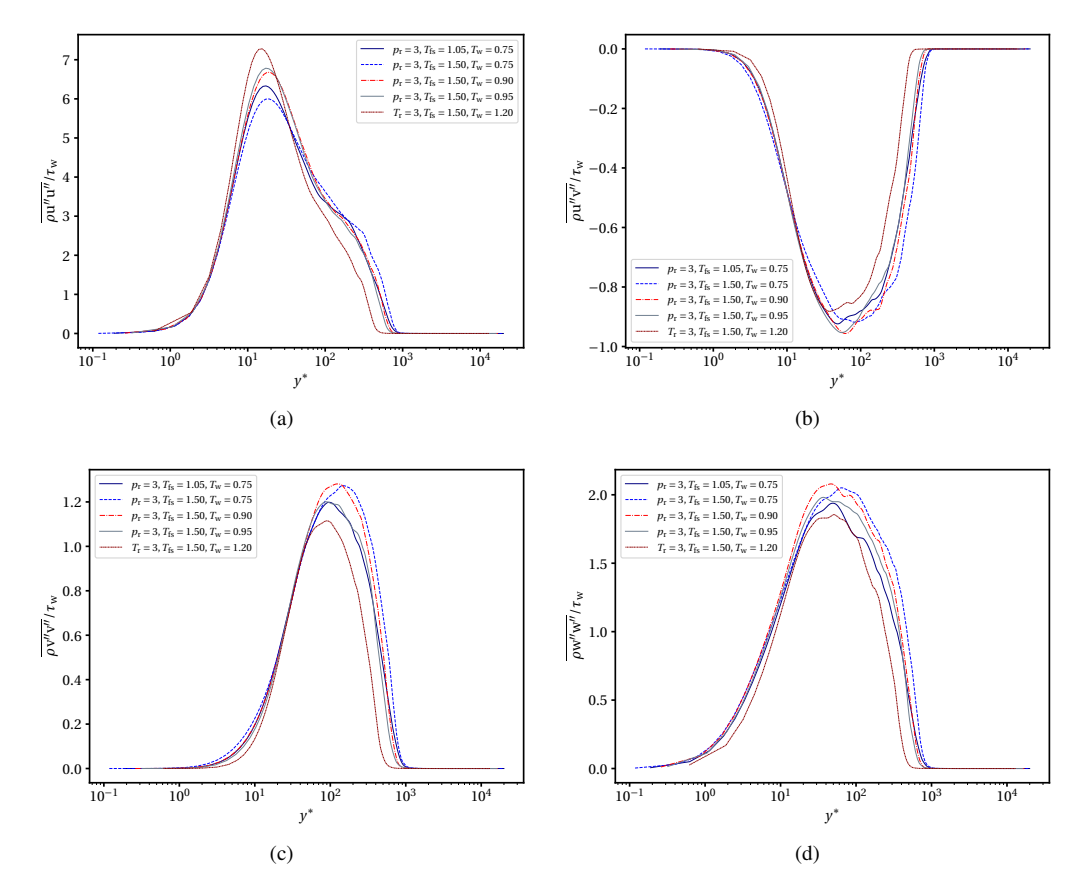


Fig. 15 Plots of normalized Favre shear stress in the boundary layers averaged over time and the z-direction.

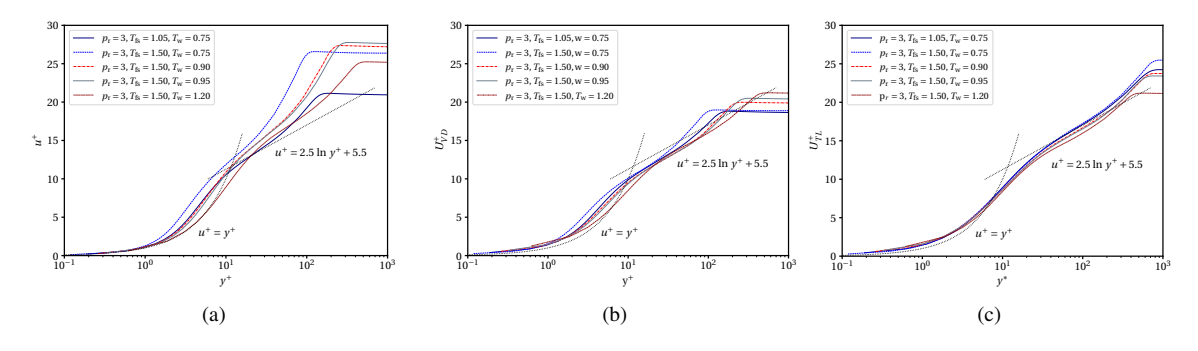


Fig. 16 Plots of scaled velocity profiles in boundary layers averaged over time and the z-direction for all five cases: (a) classical wall scaling, (b) Van Driest scaling, and (c) Trettel & Larsson scaling.

T_{∞}	1.05	1.50	1.50	1.50	1.50
T_w	0.75	0.75	0.90	0.95	1.20
$\overline{C_f}$	(0.0078, 0.0070)	(0.013, 0.012)	(0.011, 0.009)	(0.0096, 0.0086)	(0.062, 0.056)

Table 3 Range of values for the coefficient of friction (C_f) for representative regions along the streamwise direction of the boundary layers.

V. Conclusions

A set of direct numerical simulations of planar shear layer and zero-pressure-gradient boundary layer flows are performed to study the turbulent mixing of CO₂ flows in transcritical and supercritical regimes. The Peng-Robinson equation-of-state model [13] and the temperature-pressure-dependent transport models [15] are applied to characterize dense-gas behaviors. The simulations are conducted using high-order compact finite difference methods without numerical filtering or other types of excessive numerical dissipation imposed in the simulation domain of interest that suppress the growth of turbulent structures. For simulations at high Mach numbers, central-Riemann hybrid fluxes with nonlinear shock-capturing schemes are applied, and the flux blending is controlled by a localized physics-based shock sensor. The simulations of planar shear layer flows investigate turbulent mixing at two different convective Mach numbers, $M_c = 0.2$ and $M_c = 1.0$. All effects occur at a fixed freestream density ratio of 2 and reduced pressure $p_r = 3$. The simulation results indicate that the scaling of the mean velocity profile, Reynolds stress tensor, and velocity energy spectra are consistent with those of the variable density mixing in the turbulent shear layers of ideal gases. The growth of the momentum thickness at same Mach shows a similarity behavior. However, the growth of density and temperature fluctuations do not exhibit strong similarity behavior with classic scaling approaches. The compressibility factor, Z, is introduced as a scaling factor to characterize the behavior of real-gas effects. The proposed scaling achieves a significantly improved similarity behavior in the growth of pressure and temperature fluctuations at the supercritical regime. However, a The simulations of boundary layer flows investigate the effects of the presence of the Widom line within the boundary layer on mean profiles of the transport properties, thermodynamic properties, and streamwise velocity, Reynolds shear stresses, and different velocity scalings for varied wall and freestream temperatures. The results demonstrate that the presence of the Widom line causes sharp gradients in transport profiles near the wall. In addition, scalings proposed in the literature, including the classical, Van Driest, and Trettel & Larsson scalings, collapse the Reynolds shear stresses and mean velocity profiles but not as tightly as cited in the literature. This suggests that additional scaling may be necessary to account for the presence of the Widom line within the boundary layer.

VI. Acknowledgements

This work is supported by the National Science Foundation (NSF), grant number NSF-OAC-2103509. The simulation was supported by ALCC and INCITE allocations and run on the *Summit* supercomputer from the Oak Ridge Leadership Computing Facility at the Oak Ridge National Laboratory, which is supported by the Office of Science of the U.S. Department of Energy under Contract No. DE-AC05-00OR22725. A.C. is supported by the National Science Foundation Graduate Research Fellowship Program (NSF GRFP).

References

- [1] White, M. T., Bianchi, G., Chai, L., Tassou, S. A., and Sayma, A. I., "Review of supercritical CO2 technologies and systems for power generation," *Applied Thermal Engineering*, Vol. 185, 2021.
- [2] Pandey, V., Kumar, P., and Dutta, P., "Thermo-hydraulic analysis of compact heat exchanger for a simple recuperated sCO2 Brayton cycle," *Renewable and Sustainable Energy Reviews*, Vol. 134, 2020.
- [3] Cabeza, L. F., de Gracia, A., Fernández, A. I., and Farid, M. M., "Supercritical CO2 as heat transfer fluid: A review," *Applied Thermal Engineering*, Vol. 125, 2017, pp. 799–810.
- [4] Ahn, Y., Bae, S. J., Kim, M., Cho, S. K., Baik, S., Lee, J. I., and Cha, J. E., "Review of supercritical CO2 power cycle technology and current status of research and development," *Nuclear Engineering and Technology*, Vol. 47, 2015.
- [5] A.Wright, S., M.Conboy, T., and E.Rochau, G., "Supercritical CO2 power cycle development summary at sandia national laboratories," https://www.osti.gov/servlets/purl/1119778, 2011. Accessed: 2023-03-30.
- [6] C.Selle, L., A. Okongo, N., Bellan, J., and G.Harstad, K., "Modelling of subgrid-scale phenonmena in supercritical transitional mixing layers: an a priori study," *Journal of Fluid Mechanics*, Vol. 593, 2007, pp. 57–91.
- [7] Purushotham, D., A. Schau, K., and C.Oefelein, J., "Supercritical Co2 Mixing Layer," AIAA SCITECH 2022 Forum, San Diego, California, 2022.
- [8] Schmitt, T., Selle, L., Ruiz, A., and Cuenot, B., "Large-eddy simulation of supercritical-pressure round jets," *AIAA journal*, Vol. 48, No. 9, 2010, pp. 2133–2144.

- [9] Hyeon Lim, C., R.Johnston, S., and Ranjan, D., "Experimental Investigation in Turbulent Shear Mixing Layer at Supercritical Condition," *Fluids Engineering Division Summer Meeting*, Toronto, Ontario, Canada, 2022.
- [10] Manda, U., Parahovnik, A., and Peles, Y., "Theoretical Investigation of Boundary Layer Behavior and Heat Transfer of Supercritical Carbon Dioxide (sCO2) in a Microchannel," 2020 19th IEEE Intersociety Conference on Thermal and Thermomechanical Phenomena in Electronic Systems (ITherm), 2020, pp. 888–892. https://doi.org/10.1109/ITherm45881. 2020.9190408.
- [11] Manda, U., Parahovnik, A., and Peles, Y., "Theoretical Investigation of Boundary Layer Behavior and Heat Transfer of Supercritical Carbon Dioxide (sCO 2) in a Microchannel," 2020 19th IEEE Intersociety Conference on Thermal and Thermomechanical Phenomena in Electronic Systems (ITherm), IEEE, 2020, pp. 888–892.
- [12] V. Matsuno, K., and K. Lele, S., "Curvature, Variable Density, and Compressibility Effects in Turbulent Shear Layers," AIAA SCITECH 2022 Forum, San Diego, California, 2022.
- [13] Peng, D.-Y., and Robinson, D. B., "A new two-constant equation of state," *Industrial & Engineering Chemistry Fundamentals*, Vol. 15, No. 1, 1976, pp. 59–64.
- [14] WebBook, N., "Thermophysical properties of fluid systems," Avaliable Online: http://webbook. nist. gov/chemistry/fluid/(access on 18 January 2015), 2016.
- [15] Chung, T. H., Ajlan, M., Lee, L. L., and Starling, K. E., "Generalized multiparameter correlation for nonpolar and polar fluid transport properties," *Industrial & engineering chemistry research*, Vol. 27, No. 4, 1988, pp. 671–679.
- [16] Poling, B. E., Prausnitz, J. M., and O'connell, J. P., Properties of gases and liquids, McGraw-Hill Education, 2001.
- [17] Song, H., Ghate, A. S., Dai, S., Anjini, C., and Lele, S. K., "Robust high-resolution simulations of compressible turbulent flows without filtering," *AIAA Aviation 2023 Forum (currently unavailable)*, 2023.
- [18] Lele, S. K., "Compact finite difference schemes with spectral-like resolution," *Journal of computational physics*, Vol. 103, No. 1, 1992, pp. 16–42.
- [19] Nagarajan, S., Lele, S. K., and Ferziger, J. H., "A robust high-order compact method for large eddy simulation," *Journal of Computational Physics*, Vol. 191, No. 2, 2003, pp. 392–419.
- [20] Song, H., Ghate, A. S., Matsuno, K., West, J., Subramaniam, A., Brown, L. J., and Lele, S. K., "Robust high-resolution simulations of compressible turbulent flows without filtering," AIAA Aviation 2022 Forum, 2022, p. 4122.
- [21] Jiang, G.-S., and Shu, C.-W., "Efficient implementation of weighted ENO schemes," *Journal of computational physics*, Vol. 126, No. 1, 1996, pp. 202–228.
- [22] Rusanov, V. V., "The calculation of the interaction of non-stationary shock waves with barriers," *Zhurnal Vychislitel'noi Matematiki i Matematicheskoi Fiziki*, Vol. 1, No. 2, 1961, pp. 267–279.
- [23] Vadrot, A., Giauque, A., and Corre, C., "Analysis of turbulence characteristics in a temporal dense gas compressible mixing layer using direct numerical simulation," *Journal of Fluid Mechanics*, Vol. 893, 2020, p. A10.
- [24] Vadrot, A., Giauque, A., and Corre, C., "Direct numerical simulations of temporal compressible mixing layers in a Bethe–Zel'dovich–Thompson dense gas: influence of the convective Mach number," *Journal of Fluid Mechanics*, Vol. 922, 2021, p. A5.
- [25] Matsuno, K., and Lele, S. K., "Compressibility effects in high speed turbulent shear layers–revisited," *AIAA Scitech 2020 Forum*, 2020, p. 0573.
- [26] Matsuno, K., and Lele, S. K., "Variable Density Mixing in Compressible Turbulent Shear Layers," AIAA Aviation 2021 Forum, 2021, p. 2912.
- [27] Trettel, A., and Larsson, J., "Mean velocity scaling for compressible wall turbulence with heat transfer," *Physics of Fluids*, Vol. 28, No. 2, 2016.
- [28] Sciacovelli, L., Cinnella, P., and Gloerfelt, X., "Direct numerical simulations of supersonic turbulent channel flows of dense gases," *Journal of Fluid Mechanics*, Vol. 821, 2017, pp. 153–199.
- [29] Kim, K., Hickey, J.-P., and Scalo, C., "Pseudophase change effects in turbulent channel flow under transcritical temperature conditions," *Journal of Fluid Mechanics*, Vol. 871, 2019, pp. 52–91.